Materials Advances

ROYAL SOCIETY OF CHEMISTRY

PAPER

View Article Online
View Journal | View Issue

Open Access Article. Published on 21 April 2022. Downloaded on 3/10/2026 4:27:00 AM.
This article is licensed under a Creative Commons Attribution-NonCommercial 3.0 Unported Licence.

Check for updates

Cite this: *Mater. Adv.*, 2022, 3, 4381

Enhancement of the efficiency and thermal stability of the double perovskite $Cs_2AgInCl_6$ single crystal by Sc substitution†

Liyan Chen,[ab] Hangjie Jiang,[ac] Zhaohua Luo,*[a] Guoqiang Liu,[a] Xianhui Wu,[ac] Yongfu Liu,[a] Peng Sun[a] and Jun Jiang*[a]

Received 8th February 2022,
Accepted 12th April 2022

DOI: 10.1039/d2ma00139j

rsc.li/materials-advances

$Cs_2AgInCl_6$ lead-free double perovskite materials have potential applications in lighting and high-energy ray detection. However, the transition of $Cs_2AgInCl_6$ single crystals (SCs) is parity forbidden, resulting in low photoluminescence (PL) efficiency. In this study, we provide a strategy to break the parity forbidden transition by substituting Sc for In. The PL efficiency is greatly increased by 43%. In addition, the thermal stability is improved from 7.4%@475 K to 51.3%@475 K, which is attributed to the formation of Sc–Cl covalent bonds instead of In–Cl ionic ones. These results demonstrate that a suitable method makes a great contribution to promoting the possible application of $Cs_2AgInCl_6$ in the future.

Introduction

The lead-halide perovskites have recently shown tremendous application potential in solar cells, light-emitting diodes, photodetectors and lasers[1–6] due to their excellent performances, such as high photoluminescence quantum yield (PLQY), low-cost synthesis process, convenient tunability of emission colour and high tolerance to defects.[7–9] However, the toxicity of Pb and its unstable characteristics in common working conditions with a humid environment, light and high temperatures are the biggest problems hindering their commercial applications.[10–12] Therefore, it has become a focus for researchers to develop a new alternative material, which is non-toxic and chemically stable. Sn^{2+} and Ge^{2+} were first chosen to replace Pb^{2+}, but these two elements are easily oxidized into a tetravalent state, which makes the corresponding halide materials more unstable.[13]

Recently, all-inorganic lead-free double perovskites were proposed and widely studied, in which two Pb^{2+} sites were simultaneously substituted by a monovalent and a trivalent cation, abbreviated as $A_2M^+M^{3+}X_6$ (A = Cs^+; M^+ = Ag^+, Na^+ or Cu^+; M^{3+} = Bi^{3+}, In^{3+}or Sb^{3+}; X = Cl^-, Br^- or I^-).[14–18] The formation of a double perovskite structure can not only avoid toxicity, but also improve the stability of the material.[19] Among them, lead-free double perovskite $Cs_2AgInCl_6$ has attracted wide attention since it was first proposed by Volonakis *et al.*[20] This is because of its direct band gap character and suitable forbidden bandwidth, which makes rare earth and transition metal ion doping possible.[21–25] According to previous research, the luminescence mechanism of $Cs_2AgInCl_6$ is related to self-trapped excitons (STEs), arising from the strong Jahn–Teller distortion of the $AgCl_6$ octahedron.[26] This is proved by both theoretical calculations and experiments. However, the STEs and free excitons in $Cs_2AgInCl_6$ have the same orbital parity, which leads to a parity-forbidden transition.[7] As a result, $Cs_2AgInCl_6$ always suffers from a low photoluminescence quantum yield (PLQY < 0.1%). How to improve its PLQY has become one of the most important subjects to be solved.

The doping of ions is considered to be a promising method to endow and adjust the optical and optoelectronic properties of inorganic materials in the visible region.[22] Liu *et al.* increased the PLQY to 11.4% by doping Bi in $Cs_2AgInCl_6$ NCs.[27] It was also reported that Mn was doped into $Cs_2AgInCl_6$ NCs to obtain orange-red emission, and the PLQY was as high as 16%.[28] Most previous reports on $Cs_2AgInCl_6$ targeted nanocrystals. Nevertheless, the double-doped $Cs_2Ag_{0.6}Na_{0.4}InCl_6$: 0.04%Bi single crystal prepared by Luo *et al.* has bright white light emission, with a PLQY of 86.2% ± 5%. They break the parity forbidden transition by partially replacing Ag^+ with Na^+ in the $Cs_2AgInCl_6$ lattice and changing the wave function of STEs, so as to significantly improve the PL emission intensity. Furthermore, the STEs produced by the strong Jahn–Teller distortion of the $AgCl_6$ octahedron in the excited state obtain a wider visible light emission.[7]

[a] Ningbo Institute of Materials Technology and Engineering, Chinese Academy of Sciences, Ningbo 315201, China. E-mail: luozhaohua@nimte.ac.cn, jjun@nimte.ac.cn
[b] Nano Science and Technology Institute, University of Science and Technology of China, Suzhou 215123, P. R. China
[c] School of Material Science and Engineering, Jiangxi University of Science and Technology, Ganzhou, 341000, P. R. China

† Electronic supplementary information (ESI) available. See DOI: https://doi.org/10.1039/d2ma00139j

Open Access Article. Published on 21 April 2022. Downloaded on 3/10/2026 4:27:00 AM.
This article is licensed under a Creative Commons Attribution-NonCommercial 3.0 Unported Licence.

Although Na and Bi double-doped $Cs_2AgInCl_6$ single crystals have achieved excellent optical properties, previous studies mainly focused on the intrinsic band gap and photoluminescence (PL) behaviors,[20,29–31] but little on their thermal stability. In the actual application of $Cs_2AgInCl_6$ materials, not only the luminescence properties, such as quantum yield, but also stability must be considered, and thermal stability is an extremely important aspect.

Inspired by these results, we propose for the first time to dope Scandium (Sc) into $Cs_2AgInCl_6$, with the aim to improve its PL efficiency and thermal stability. On the one hand, Sc^{3+} ions have the same valence state and similar ionic radius as that of In^{3+}, which makes it possible to be alloyed into $Cs_2AgInCl_6$, and subsequently, its PL efficiency would be improved by the broken symmetry of the crystal structure. More importantly, when Sc^{3+} is doped, the electrons on the Sc d orbital and those on the Cl p orbital tend to form a covalent bond-like structure. Therefore, the thermal stability of $Cs_2AgIn_{1-x}Sc_xCl_6$ ($x > 0$) would be effectively improved. We believe that the alloying of Sc^{3+} would prove to be a new way to help to promote the real application of $Cs_2AgInCl_6$.

Results and discussion

1. Morphology and crystal structure of $Cs_2AgIn_{1-x}Sc_xCl_6$

Fig. S1 (ESI†) presents the picture of the $Cs_2AgInCl_6$ crystal, which exhibits a regular octahedral shape with a size of about 1 mm. To confirm the crystalline character, the powder X-ray diffraction (XRD) patterns of $Cs_2AgIn_{1-x}Sc_xCl_6$ (x = 0, 0.2, 0.4, 0.6, 0.8 and 1) are collected and shown in Fig. 1a. It is found that almost all the peaks match well with the reference standard pattern ($Cs_2AgInCl_6$, (ICSD-244519)) when the Sc doping amount $x \leq 0.4$, indicating that Sc^{3+} ions have entered the lattice and formed a solid solution with the $Cs_2AgInCl_6$ substrate. In addition, from the enlarged view of the characteristic (220) diffraction peak as shown in Fig. 1a, it also can be found that the diffraction peak shifts to a higher angle as the amount of x increases from 0 to 0.8. Noted that, the ionic radius for 6-coordinated Sc^{3+} (r = 0.745 Å) is slightly smaller than that of In^{3+} (r = 0.8 Å). According to the Bragg equation, the substitution of Sc^{3+} for In^{3+} would cause shrinkage of the lattice and result in a peak shift towards a larger angle, which is supported by the results of the calculated lattice constant as shown in Fig. 1b. However, when the amount of Sc^{3+} is more than 60% (x = 0.6), the AgCl second phase appears, and only the AgCl phase can be found when x = 1, which means that the solid solubility of Sc^{3+} in the $Cs_2AgInCl_6$ lattice is less than 60%.

In order to clarify the influence of Sc^{3+} ions on the crystal structure, samples of $Cs_2AgInCl_6$, $Cs_2AgIn_{0.8}Sc_{0.2}Cl_6$, $Cs_2AgIn_{0.6}Sc_{0.4}Cl_6$ and $Cs_2AgIn_{0.4}Sc_{0.6}Cl_6$ are taken for further XRD measurement and refined by Rietveld refinement, as presented in Fig. S2 (ESI†). The detailed structure parameters of $Cs_2AgIn_{1-x}Sc_xCl_6$ (x = 0, 0.2, 0.4 and 0.6) determined with Rietveld refinement and the reliability factors are listed in Table S1 (ESI†). The reliability factors in Table S1 (ESI†) indicate that the results of Rietveld refinements are reliable. According to the Rietveld refinement results, $Cs_2AgIn_{1-x}Sc_xCl_6$ (x = 0, 0.2, 0.4 and 0.6) belongs to the cubic crystal system with the $Fm\bar{3}m$ space group. Moreover, the cell parameter decreases from 10.502 Å to 10.495 Å with the introduction of 60% Sc^{3+} (x = 0.6) ions, as plotted in Fig. 1b. It should be noted that, according to the results of Rietveld refinement, the occupancies of Sc^{3+} in In^{3+} sites are much less than the designed values (as shown in Table S1, ESI†).

To identify the composition uniformity, the $Cs_2AgIn_{0.6}Sc_{0.4}Cl_6$ single-crystal particle with extremely small size was selected and analyzed by EDS-mapping, which is given in Fig. 2. As shown in the SEM image of Fig. 2a, the $Cs_2AgIn_{0.6}Sc_{0.4}Cl_6$ single-crystal presents a regular octahedron morphology. The pictures of EDS mapping show that Cs, Ag, In, Cl and Sc elements are homogeneously distributed within the selected particle. However, the Sc

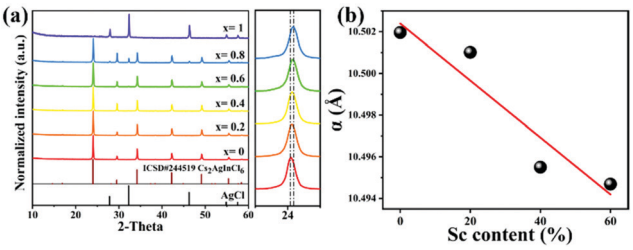

Fig. 1 (a) XRD patterns and selected diffraction peaks at around 24° of the as-prepared $Cs_2AgIn_{1-x}Sc_xCl_6$ (x = 0, 0.2, 0.4, 0.6, 0.8 and 1), and (b) the change of cell parameters with Sc doping content.

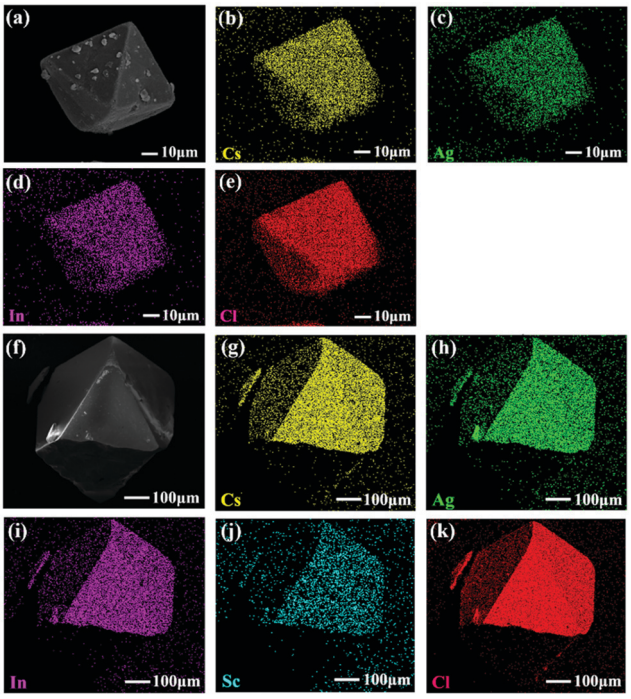

Fig. 2 (a) SEM image of the $Cs_2AgInCl_6$ SC. (b–e) EDS-mapping of Cs, Ag, In and Cl for the selected $Cs_2AgInCl_6$ particle. (f) SEM image of the $Cs_2AgIn_{0.6}Sc_{0.4}Cl_6$ SC. (g–k) EDS-mapping of Cs, Ag, In, Sc and Cl for the selected $Cs_2AgIn_{0.6}Sc_{0.4}Cl_6$ particle.

 © 2022 The Author(s). Published by the Royal Society of Chemistry

Open Access Article. Published on 21 April 2022. Downloaded on 3/10/2026 4:27:00 AM.
This article is licensed under a Creative Commons Attribution-NonCommercial 3.0 Unported Licence.

intensity is very weak, which is consistent with the results of Rietveld refinement as shown in Table S1 (ESI†).

2. Spectral characteristics of $Cs_2AgIn_{1-x}Sc_xCl_6$ single crystals

With the aim to understand the effect of Sc^{3+} doping on the optical properties of $Cs_2AgInCl_6$, the normalized steady-state absorption spectra of $Cs_2AgIn_{1-x}Sc_xCl_6$ single crystals with x varying from 0 to 0.6 are measured and shown in Fig. 3a. As for $Cs_2AgInCl_6$, a sharp absorption edge starting at around 400 nm is observed, which is attributed to the allowed transition and consistent with the previous reports. With the increase of the Sc doping level, this absorption edge shifts to a longer wavelength. In addition, there is another broad absorption with the edge starting around 900 nm for samples with Sc doping. The absorption intensity enhanced, and the absorption edges of $Cs_2AgIn_{1-x}Sc_xCl_6$ broadened with the increase of the Sc content. In order to determine the optical bandgaps of $Cs_2AgIn_{1-x}Sc_xCl_6$ crystals, the following equation was used:

$$[F(R_\infty)*h\nu]^n = A(h\nu - E_g) \quad (1)$$

where $h\nu$ is the photon energy; A is a proportional constant; E_g represents the value of the band gap; n = 2 since the $Cs_2AgIn\,Cl_6$ host absorption is a direct transition; and $F(R_\infty)$ is the Kubelka–Munk function defined as:

$$F(R_\infty) = (1 - R)^2/R \quad (2)$$

where R represents the reflection coefficient.[32] Tauc plots of $Cs_2AgIn_{1-x}Sc_xCl_6$ single crystals (x = 0, 0.2, 0.4 and 0.6) are presented in Fig. 3b. It shows that the indirect bandgap appears with the doping of Sc^{3+}, and it increases from 1.0 to 1.18 eV as the amount of Sc^{3+} increases from 0.2 to 0.6. The variation of the bandgaps would be attributed to the change in electronic structure that we will discuss in the next section. In addition, with the increase in the Sc doping level, the energy difference from the VBM to the second conduction band decreases from 3.29 eV for $Cs_2AgInCl_6$ to 2.44 eV for $Cs_2AgIn_{0.4}Sc_{0.6}Cl_6$.

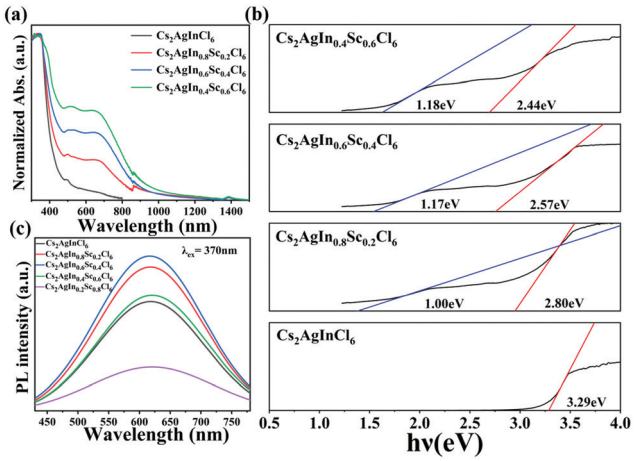

Fig. 3 The normalized steady-state absorption spectra (a), the Tauc plot of $Cs_2AgIn_{1-x}Sc_xCl_6$ (x = 0, 0.2, 0.4, 0.6 and 0.8) single crystals (b), and photoluminescence (PL) spectra (c).

The steady-state photoluminescence spectra of the $Cs_2AgIn_{1-x}Cl_6$: xSc^{3+} samples are shown in Fig. 3c. Excited by ultraviolet radiation of 370 nm, all samples exhibit broadband emission character with a peak at around 620 nm, and the position of these peaks is almost unchanged upon tuning the content of Sc (as shown in Fig. S4, ESI†). In general, the broadband emission usually comes from STEs or excited state reorganization, which exists in semiconductors with localized carriers and soft crystal lattices, as reported previously.[33–36] The STEs that exist in $Cs_2AgInCl_6$ crystals are thought to be caused by the Jahn–Teller distortion of the $AgCl_6$ octahedron, which emits effectively and stably. Moreover, the integral intensity for the PL spectra increases at first and then decreases with a maximum increment of 43% when x = 0.4 (as shown in Fig. S4, ESI†). The reason can be attributed to the octahedral $AgCl_6$ distortion with the doping of Sc, which would help to break the reverse symmetry and modify the parity forbidden transition subsequently.

3. Electronic structure of $Cs_2AgScCl_6$ single crystals

In order to have a deeper understanding of the changes brought about by Sc doping, we analyze the electronic structure of $Cs_2AgScCl_6$, as shown in Fig. 4.

Fig. 4a and b, respectively, present the calculated band structure and density of states (DOS) for $Cs_2AgScCl_6$. The calculations were performed using the full-potential package of WIEN2K with an 8 × 8 × 8 K-point mesh. The previous theoretical calculation indicated that $Cs_2AgInCl_6$ is a direct gap semiconductor.[29] Fig. 4a shows that $Cs_2AgScCl_6$ is an indirect semiconductor, while the valence band maximum (VBM) and conduction band minimum (CBM) appear at the L and X points, respectively. The obtained band gap is about 2.5 eV, which is smaller than that of $Cs_2AgInCl_6$ in the previous report.[27,37–39] Therefore, it is reasonable to deduce that the direct bandgap of $Cs_2AgInCl_6$ would decrease with the doping of Sc and that is in accordance with our results as shown in Fig. 3b.

The DOS of $Cs_2AgScCl_6$ and the partial DOS for Sc are displayed in Fig. 4b. As may be seen, the conduction band around 3 eV is mainly from the orbital of Sc. As for a pure Sc^{3+} ion, its d-orbital should be fully empty and is located at the position of the conduction band. However, the partial DOS of Sc shows a peak around −3.5 eV. This fact indicates that Sc-d and Cl-p orbitals form a valence bond rather than an ionic

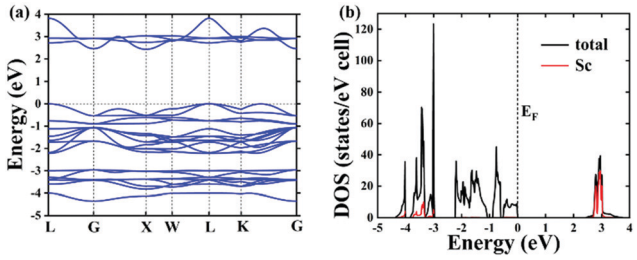

Fig. 4 The calculated band structure (a), and density of states (b) for $Cs_2AgScCl_6$.

Open Access Article. Published on 21 April 2022. Downloaded on 3/10/2026 4:27:00 AM.
This article is licensed under a Creative Commons Attribution-NonCommercial 3.0 Unported Licence.

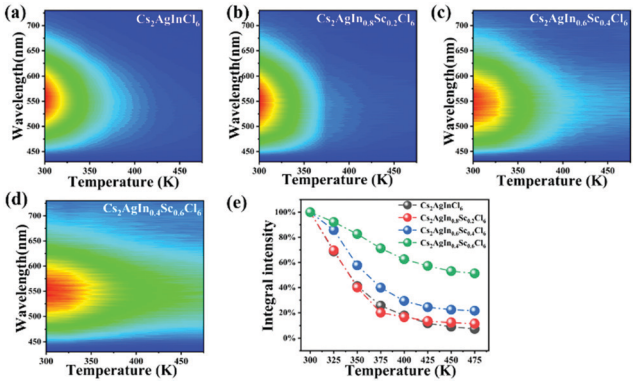

Fig. 5 Temperature-dependent PL spectra (a–d) and the relationship between PL intensity and temperature for $Cs_2AgIn_{0.8}Sc_{0.2}Cl_6$, $Cs_2AgIn_{0.6}Sc_{0.4}Cl_6$ and $Cs_2AgIn_{0.4}Sc_{0.6}Cl_6$, respectively (e).

bond. Usually, the bond strength of valence bonding is stronger than ionic bonding.[40,41] For this reason, the lattice constant of $Cs_2AgScCl_6$ is decreased relative to $Cs_2AgInCl_6$, and the thermal stability would also be improved.

4. Thermal stability of $Cs_2AgIn_{1-x}Sc_xCl_6$ single crystals

In real applications, such as solar photovoltaics and semiconductor lighting, heat generation in photoelectric conversion materials is unavoidable. As a result, it requires the materials to have robust thermal stability, which was often neglected in the past. The temperature-dependent PL spectra of $Cs_2AgIn_{1-x}Sc_xCl_6$ (x = 0, 0.2, 0.4 and 0.6) single crystals are shown in Fig. 5a–d, where a slight blue shift is observed for the emission peaks upon the increase of the temperature (as shown in Fig. S5, ESI†). Here, we consider that both electron–phonon interaction and crystal lattice thermal expansion would be responsible for this blue shift, and a similar phenomenon has been observed in lead/copper chalcogenide semiconductors and lead-halide perovskites.[42–44]

To clarify the thermal stability of $Cs_2AgIn_{1-x}Sc_xCl_6$ single crystals, the relationship between integral PL intensities and temperature is presented in Fig. 5e. It clearly shows that the emission intensity decreases with the rise of temperature, owing to the thermally activated nonradiative recombination. Moreover, it can also be observed that the rate of PL intensity decline slows down with the increase of Sc doping concentration, indicating that the thermal stability is effectively improved. For example, the PL intensity of $Cs_2AgIn_{0.4}Sc_{0.6}Cl_6$ at 475 K still maintained 51.3% of that at room temperature, while the PL intensity of $Cs_2AgInCl_6$ only maintained 7.4%. There are mainly two reasons for this enhancement. First, the electrons on the In-s orbital and Cl-p orbital in $Cs_2AgInCl_6$ are usually in the form of ionic bonds, but when Sc^{3+} is doped, electrons on the Sc-d orbital and Cl-p orbital tend to form a structure similar to a covalent bond, which is pointed out in the analysis of the DOS results in the previous section. Second, the incorporation of Sc^{3+} causes the contraction of the $Cs_2AgInCl_6$ crystal lattice, and the bond length becomes shorter. As a result, the interaction between ions would be enhanced, and the rigidity of the crystal lattice will be improved.

Conclusions

In conclusion, Sc-alloyed $Cs_2AgInCl_6$ SCs have been successfully synthesized by hydrothermal synthesis. Results of Rietveld refinement show that Sc^{3+} ions take the place of In^{3+} sites, but their actual occupancies are considerably lower than the designed values. With the incorporation of Sc, the PL intensity of $Cs_2AgInCl_6$ SCs can be enhanced by 43%. This may be caused by the local structure distortion that would break the reverse symmetry and subsequently modify the parity forbidden transition of STEs. In addition, the thermal stability of $Cs_2AgInCl_6$ is also enhanced with the doping of Sc. The PL intensity of $Cs_2AgIn_{0.4}Sc_{0.6}Cl_6$ at 475 K is 51.3% of that at room temperature, while it drops to 7.4% for $Cs_2AgInCl_6$. According to the calculated results of electronic structure, the enhancement of the thermal stability is attributed to the formation of a covalent bond for Sc–Cl other than the ionic bond for In–Cl. There is a reason to believe that the Sc doping would provide an effective solution to enhance the problems of low PL and thermal stability for $Cs_2AgInCl_6$ single crystals.

Experimental section

Materials

Silver chloride (AgCl, 99.5%), sodium chloride (NaCl, 99.99%), anhydrous indium chloride ($InCl_3$, 99.99%), hydrochloric acid and isopropanol were purchased from Aladdin. Cesium chloride (CsCl, AR) and scandium nitrate hydrate ($Sc(NO_3)_3$, 99.9%) were purchased from Macklin. All chemicals were used without any further purification.

Synthesis of $Cs_2AgIn_{1-x}Sc_xCl_6$ single crystals

1 mmol of AgCl, $1 - x$ mmol of anhydrous $InCl_3$, x mmol Sc $(NO_3)_3$ and 2 mmol of CsCl were first dissolved in 10 ml M HCl solution in a beaker. After stirring for 30 minutes, the solution was then transferred to a 25 ml Teflon autoclave. The Teflon autoclave was heated at 180 °C for 12 h in a stainless steel Parr Auto-Claveand, and then, the solution was stably cooled to 50 °C at a speed of 5 °C h^{-1}. The as-prepared crystals were then filtered out, washed twice with isopropanol and dried in a furnace at 65 °C.

Characterization

Powder XRD measurements were performed by grinding Cs_2AgIn_{1-x} Sc_xCl_6 crystals into fine powders in a mortar, and then using a Bruker D8 X-ray diffractometer with Cu Kα radiation (λ = 1.54056 Å) at 40 kV and 40 mA. The crystal structures were determined with Rietveld refinement by using a general structure analysis system (GSAS).[45] A field-emission scanning electron microscope (FE-SEM, Hitachi S-4800) equipped with an energy-dispersive X-ray spectroscopy (EDS) system was used to measure the morphology. The photoluminescence and PLE measurements were carried out using a Horiba FL3-111 fluorescence spectrometer with a xenon lamp as a light source. The temperature-dependent photoluminescence spectra were measured using the same instrument excited by a 360 nm wavelength

 © 2022 The Author(s). Published by the Royal Society of Chemistry

Open Access Article. Published on 21 April 2022. Downloaded on 3/10/2026 4:27:00 AM. This article is licensed under a Creative Commons Attribution-NonCommercial 3.0 Unported Licence.

and at a temperature ranging from 300 to 475 K. The absorption spectra were measured at room temperature using a LAMBDA 950 ultraviolet-visible-near infrared spectrophotometer.

Author contributions

Liyan Chen: investigation, validation, formal analysis, data curation, writing – original draft; Hangjie Jiang: investigation, data curation; Zhaohua Luo: investigation, data curation, writing – review & editing, funding acquisition, supervision; Guoqiang Liu: investigation, data curation; Xianhui Wu: data curation; Yongfu Liu: investigation, data curation, funding acquisition; Peng Sun: investigation, data curation; Jun Jiang: resources, writing – review & editing, supervision, funding acquisition, project administration.

Conflicts of interest

There are no conflicts of interest to declare.

Acknowledgements

This work is financially supported by the "Pioneer" and "Leading Goose" R&D Program of Zhejiang (2022C01046), and the National Natural Science Foundation of China (12074393, 62105342).

References

1 L. Protesescu, S. Yakunin, M. I. Bodnarchuk, F. Krieg, R. Caputo, C. H. Hendon, R. X. Yang, A. Walsh and M. V. Kovalenko, *Nano Lett.*, 2015, **15**, 3692–3696.
2 H. Huang, M. I. Bodnarchuk, S. V. Kershaw, M. V. Kovalenko and A. L. Rogach, *ACS Energy Lett.*, 2017, **2**, 2071–2083.
3 R. E. Brandt, J. R. Poindexter, P. Gorai, R. C. Kurchin, R. L. Z. Hoye, L. Nienhaus, M. W. B. Wilson, J. A. Polizzotti, R. Sereika, R. Zaltauskas, L. C. Lee, J. L. MacManus-Driscoll, M. Bawendi, V. Stevanovic and T. Buonassisi, *Chem. Mater.*, 2017, **29**, 4667–4674.
4 J. Kang and L. W. Wang, *J. Phys. Chem. Lett.*, 2017, **8**, 489–493.
5 Z. Jia, C. Yuan, Y. Liu, X. J. Wang, P. Sun, L. Wang, H. Jiang and J. Jiang, *Light: Sci. Appl.*, 2020, **9**, 86.
6 Q. Yao, P. Hu, P. Sun, M. Liu, R. Dong, K. Chao, Y. Liu, J. Jiang and H. Jiang, *Adv. Mater.*, 2020, **32**, e1907888.
7 J. Luo, X. Wang, S. Li, J. Liu, Y. Guo, G. Niu, L. Yao, Y. Fu, L. Gao, Q. Dong, C. Zhao, M. Leng, F. Ma, W. Liang, L. Wang, S. Jin, J. Han, L. Zhang, J. Etheridge, J. Wang, Y. Yan, E. H. Sargent and J. Tang, *Nature*, 2018, **563**, 541–545.
8 Y. Luo, N. Liu, X. Li, J. C. Hone and S. Strauf, *2D Mater.*, 2019, 6.
9 X. Wang, W. Meng, W. Liao, J. Wang, R. G. Xiong and Y. Yan, *J. Phys. Chem. Lett.*, 2019, **10**, 501–506.
10 C. Bi, S. V. Kershaw, A. L. Rogach and J. Tian, *Adv. Funct. Mater.*, 2019, 29.
11 Y. Wei, Z. Cheng and J. Lin, *Chem. Soc. Rev.*, 2019, **48**, 310–350.
12 H. C. Wang, S. Y. Lin, A. C. Tang, B. P. Singh, H. C. Tong, C. Y. Chen, Y. C. Lee, T. L. Tsai and R. S. Liu, *Angew. Chem., Int. Ed.*, 2016, **55**, 7924–7929.
13 S. Ghosh and B. Pradhan, *ChemNanoMat*, 2019, **5**, 300–312.
14 Q. A. Akkerman, G. Raino, M. V. Kovalenko and L. Manna, *Nat. Mater.*, 2018, **17**, 394–405.
15 F. Wei, Z. Deng, S. Sun, F. Zhang, D. M. Evans, G. Kieslich, S. Tominaka, M. A. Carpenter, J. Zhang, P. D. Bristowe and A. K. Cheetham, *Chem. Mater.*, 2017, **29**, 1089–1094.
16 Z. W. Xiao, W. W. Meng, J. B. Wang, D. B. Mitzi and Y. F. Yan, *Mater. Horiz.*, 2017, **4**, 206–216.
17 A. H. Slavney, T. Hu, A. M. Lindenberg and H. I. Karunadasa, *J. Am. Chem. Soc.*, 2016, **138**, 2138–2141.
18 D. H. Fabini, T. Hogan, H. A. Evans, C. C. Stoumpos, M. G. Kanatzidis and R. Seshadri, *J. Phys. Chem. Lett.*, 2016, **7**, 376–381.
19 K. Dave, M. H. Fang, Z. Bao, H. T. Fu and R. S. Liu, *Chem. – Asian J.*, 2020, **15**, 242–252.
20 G. Volonakis, A. A. Haghighirad, R. L. Milot, W. H. Sio, M. R. Filip, B. Wenger, M. B. Johnston, L. M. Herz, H. J. Snaith and F. Giustino, *J. Phys. Chem. Lett.*, 2017, **8**, 772–778.
21 Y. Mahor, W. J. Mir and A. Nag, *J. Phys. Chem. C*, 2019, **123**, 15787–15793.
22 Y. Liu, X. Rong, M. Li, M. S. Molokeev, J. Zhao and Z. Xia, *Angew. Chem., Int. Ed.*, 2020, **59**, 11634–11640.
23 Z. Zeng, B. Huang, X. Wang, L. Lu, Q. Lu, M. Sun, T. Wu, T. Ma, J. Xu, Y. Xu, S. Wang, Y. Du and C. H. Yan, *Adv. Mater.*, 2020, **32**, 2004506.
24 Q. Liao, J. Chen, L. Zhou, T. Wei, L. Zhang, D. Chen, F. Huang, Q. Pang and J. Z. Zhang, *J. Phys. Chem. Lett.*, 2020, **11**, 8392–8398.
25 P. Han, X. Zhang, C. Luo, W. Zhou, S. Yang, J. Zhao, W. Deng and K. Han, *ACS Cent. Sci.*, 2020, **6**, 566–572.
26 Y. Liu, A. Nag, L. Manna and Z. Xia, *Angew. Chem., Int. Ed.*, 2021, **60**, 11592–11603.
27 Y. Liu, Y. Jing, J. Zhao, Q. Liu and Z. Xia, *Chem. Mater.*, 2019, **31**, 3333–3339.
28 W. Lee, S. Hong and S. Kim, *J. Phys. Chem. C*, 2019, **123**, 2665–2672.
29 J. Zhou, Z. G. Xia, M. S. Molokeev, X. W. Zhang, D. S. Peng and Q. L. Liu, *J. Mater. Chem. A*, 2017, **5**, 15031–15037.
30 J. Luo, S. Li, H. Wu, Y. Zhou, Y. Li, J. Liu, J. Li, K. Li, F. Yi, G. Niu and J. Tang, *ACS Photonics*, 2017, **5**, 398–405.
31 T. T. Tran, J. R. Panella, J. R. Chamorro, J. R. Morey and T. M. McQueen, *Mater. Horiz.*, 2017, **4**, 688–693.
32 F. Y. Zhao, Z. Song, J. Zhao and Q. L. Liu, *Inorg. Chem. Front.*, 2019, **6**, 3621–3628.
33 Z. Yuan, C. Zhou, Y. Tian, Y. Shu, J. Messier, J. C. Wang, L. J. van de Burgt, K. Kountouriotis, Y. Xin, E. Holt, K. Schanze, R. Clark, T. Siegrist and B. Ma, *Nat. Commun.*, 2017, **8**, 14051.

Open Access Article. Published on 21 April 2022. Downloaded on 3/10/2026 4:27:00 AM.
This article is licensed under a Creative Commons Attribution-NonCommercial 3.0 Unported Licence.

34 C. Zhou, Y. Tian, Z. Yuan, H. Lin, B. Chen, R. Clark, T. Dilbeck, Y. Zhou, J. Hurley, J. Neu, T. Besara, T. Siegrist, P. Djurovich and B. Ma, *ACS Appl. Mater. Interfaces*, 2017, **9**, 44579–44583.
35 C. Zhou, Y. Tian, M. Wang, A. Rose, T. Besara, N. K. Doyle, Z. Yuan, J. C. Wang, R. Clark, Y. Hu, T. Siegrist, S. Lin and B. Ma, *Angew. Chem., Int. Ed.*, 2017, **56**, 9018–9022.
36 C. Zhou, H. Lin, Y. Tian, Z. Yuan, R. Clark, B. Chen, L. J. van de Burgt, J. C. Wang, Y. Zhou, K. Hanson, Q. J. Meisner, J. Neu, T. Besara, T. Siegrist, E. Lambers, P. Djurovich and B. Ma, *Chem. Sci.*, 2018, **9**, 586–593.
37 J. C. Dahl, W. T. Osowiecki, Y. Cai, J. K. Swabeck, Y. Bekenstein, M. Asta, E. M. Chan and A. P. Alivisatos, *Chem. Mater.*, 2019, **31**, 3134–3143.
38 B. Nath, B. Pradhan and S. K. Panda, *New J. Chem.*, 2020, **44**, 18656–18661.
39 P. G. Han, X. Zhang, X. Mao, B. Yang, S. Q. Yang, Z. C. Feng, D. H. Wei, W. Q. Deng, T. Pullerits and K. L. Han, *Sci. China: Chem.*, 2019, **62**, 1405–1413.
40 A. Burawoy, *Trans. Faraday Soc.*, 1943, **39**, 79–90.
41 H. A. Skinner, *Thermochim. Acta*, 1986, **109**, 165–174.
42 S. Li, H. Y. Wang, P. Yang, L. L. Wang, X. R. Cheng and K. Yang, *J. Alloys Compd.*, 2021, 854.
43 P. Dey, J. Paul, J. Bylsma, D. Karaiskaj, J. M. Luther, M. C. Beard and A. H. Romero, *Solid State Commun.*, 2013, **165**, 49–54.
44 Y. Li, Z. F. Shi, L. Z. Lei, F. Zhang, Z. Z. Ma, D. Wu, T. T. Xu, Y. T. Tian, Y. T. Zhang, G. T. Du, C. X. Shan and X. J. Li, *Chem. Mater.*, 2018, **30**, 6744–6755.
45 Z. H. Luo, Y. F. Liu, C. H. Zhang, J. X. Zhang, H. M. Qin, H. C. Jiang and J. Jiang, *Inorg. Chem.*, 2016, **55**, 3040–3046.

 © 2022 The Author(s). Published by the Royal Society of Chemistry